

PAPER

## Carrier confinement effects observed in the normal-state electrical transport of electron-doped cuprate trilayers

To cite this article: Chiara Sacco *et al* 2019 *J. Phys. D: Appl. Phys.* **52** 135303

View the [article online](#) for updates and enhancements.




**IOP | ebooks™**

Bringing you innovative digital publishing with leading voices to create your essential collection of books in STEM research.

Start exploring the collection - download the first chapter of every title for free.

# Carrier confinement effects observed in the normal-state electrical transport of electron-doped cuprate trilayers

Chiara Sacco<sup>1,2</sup> , Alice Galdi<sup>1,2,3</sup>, Francesco Romeo<sup>4</sup>, Nunzia Coppola<sup>1,2</sup>, Pasquale Orgiani<sup>2</sup>, Haofei I Wei<sup>5</sup>, Berit H Goodge<sup>6,7</sup>, Lena F Kourkoutis<sup>6,7</sup>, Kyle Shen<sup>5,7</sup>, Darrell G Schlom<sup>7,8</sup> and Luigi Maritato<sup>1,2</sup>

<sup>1</sup> Dipartimento di Ingegneria Industriale-DIIN, Università degli Studi di Salerno, Fisciano, SA 84084, Italy

<sup>2</sup> CNR SPIN u.o.s. Salerno, Fisciano, SA 84084, Italy

<sup>3</sup> CLASSE, Cornell University, Ithaca, NY 14853, United States of America

<sup>4</sup> Dipartimento di Fisica 'E.R. Caianiello', Università degli Studi di Salerno, Fisciano, SA 84084, Italy

<sup>5</sup> Department of Physics, Cornell University, Ithaca, NY 14853, United States of America

<sup>6</sup> School of Applied and Engineering Physics, Cornell University, Ithaca, NY 14853, United States of America

<sup>7</sup> Kavli Institute at Cornell for Nanoscale Science, Ithaca, NY 14853, United States of America

<sup>8</sup> Department of Material Science and Engineering, Cornell University, Ithaca, NY 14853, United States of America

E-mail: [chsacco@unisa.it](mailto:chsacco@unisa.it)

Received 16 September 2018, revised 14 January 2019

Accepted for publication 17 January 2019

Published 1 February 2019



## Abstract

SrCuO<sub>2</sub>/Sr<sub>0.9</sub>La<sub>0.1</sub>CuO<sub>2</sub>/SrCuO<sub>2</sub> trilayers were grown by oxide-molecular beam epitaxy. The thicknesses of the top and bottom SrCuO<sub>2</sub> layers were fixed, while the thickness of the infinite-layer electron-doped cuprate Sr<sub>0.9</sub>La<sub>0.1</sub>CuO<sub>2</sub> central layer was systematically changed. Transmission electron microscopy, x-ray reflectivity and x-ray diffraction measurements were performed to assess the sample quality and the abruptness of the interfaces. Electrical transport measurements as a function of temperature and as a function of central layer thickness, confirm that the normal state properties of the trilayers are altered by the confinement of the charge carriers in the central layer.

Keywords: interfaces, molecular beam epitaxy, quantum wells, electron-doped cuprates, oxides

(Some figures may appear in colour only in the online journal)

## 1. Introduction

Driven by important developments in oxide thin film deposition techniques, low-dimensional transition-metal oxides (TMO) heterostructures have shown many fascinating and exotic behaviours at complex oxide interfaces [1–8]. Advances in oxide-molecular beam epitaxy (O-MBE) techniques [9–12], i.e. atomic-scale thickness control, abrupt interfaces and the possibility to change the chemical composition over a distance of a single unit cell, have allowed the growth of epitaxial oxide thin films and oxide-based heterostructures with

performances comparable to those of the best conventional semi-conductor systems, opening a path to the fabrication of oxide-based quantum well (QW) devices.

An oxide based QW is the simplest system in which quantum confinement can be obtained. It consists of three layers with the conducting oxide sandwiched between two layers of insulating oxide material. Several oxide-based QWs have been studied, such as SrTiO<sub>3</sub>/SrVO<sub>3</sub>/SrTiO<sub>3</sub>, GdTiO<sub>3</sub>/SrTiO<sub>3</sub>/GdTiO<sub>3</sub> and SmTiO<sub>3</sub>/SrTiO<sub>3</sub>/SmTiO<sub>3</sub> [13–16]. In these systems the carrier concentration of the conducting layer was not systematically varied. In view of potential

applications, it is highly desirable to have the possibility to vary both the thickness of the QW and the density of charge carriers it contains. It is prudent, especially from an experimental perspective when depositing QWs using O-MBE, to minimize the number of different materials (sources) involved in the deposition. As many TMO are Mott insulators with small energy band gaps, the question arises whether they can effectively be used to obtain charge confinement in QWs. Recently, *p*-type SrMnO<sub>3</sub>/La<sub>0.7</sub>Sr<sub>0.3</sub>MnO<sub>3</sub>/SrMnO<sub>3</sub> (SMO/LSMO/SMO) QWs have been grown by a shuttered layer-by-layer O-MBE deposition technique in which the monolayer dose times were calibrated by shuttered reflection high energy electron diffraction (RHEED) oscillations. The electrical transport properties of these films have been characterized as a function of temperature and also as a function of the thickness of the La<sub>0.7</sub>Sr<sub>0.3</sub>MnO<sub>3</sub> central layers [17]. The results confirm the confinement of charge carriers in the trilayers investigated, pointing out that a small gap Mott insulator, such as SrMnO<sub>3</sub> ( $E_g = 0.35$  eV) [18], can be successfully used in QW structures as barriers. The availability of both *p* and *n* doped oxide QWs grown by the same deposition technique under similar deposition conditions, involving a minimum number of materials, is key to obtaining *p-n* TMO based proximate structures [19, 20].

Building upon our previous work on the growth and characterization of infinite layer (IL) electron-doped Sr<sub>1-x</sub>La<sub>x</sub>CuO<sub>2</sub> epitaxial thin films by a shuttered layer-by-layer O-MBE RHEED calibrated deposition process [7, 17, 21, 22], here we study the effects of confinement of the central layer on the normal state transport properties of SrCuO<sub>2</sub>/Sr<sub>0.9</sub>La<sub>0.1</sub>CuO<sub>2</sub>/SrCuO<sub>2</sub> (SCO/SLCO/SCO) electron-doped trilayers as a function of thickness of the SLCO central layer. The IL tetragonal SCO, with only one Cu–O plane per unit cell and without oxygen atoms in the Sr layers, is the simplest undoped parent structure in the cuprate family that exhibits high-critical temperature ( $T_C$ ) superconductivity. Partial substitution of La<sup>3+</sup> for Sr<sup>2+</sup> yields an *n*-type compound with  $T_C$  up to about 40 K [23].

Scanning transmission electron microscopy (STEM) and x-ray diffraction (XRD) analysis provided evidence of epitaxial growth with atomically abrupt interfaces. Electrical transport results in the normal state exhibit a dependence on the thickness of the central SLCO layer that is mainly induced by the presence of clean interfaces with the confinement layers. The results provide new hints in the understanding of low dimensional *n*-doped cuprate systems and in the growth of *p-n* doped oxide based proximate structures involving a minimum number of different materials.

## 2. Experimental results

(SCO)<sub>20</sub>/(SLCO)<sub>*y*</sub>/(SCO)<sub>15</sub> (with  $y = 20, 15, 10, 5, 4, 3$ , where  $y$  is the thickness of the SLCO in unit cells (u.c.) and 20 and 15 are the thickness of the bottom and top SCO layers in u.c., respectively) samples were grown in a Veeco-GEN10 dual-chamber oxide MBE system using a shuttered layer-by-layer deposition process performed in purified O<sub>3</sub> at

a background pressure of  $3 \times 10^{-7}$  Torr. The films were deposited on (1 1 0) TbScO<sub>3</sub> (TSO) substrates which have an orthorhombical distorted perovskite structure (pseudo-cubic lattice parameter 0.3958 nm). Both the SLCO and the SCO layers (with bulk in-plane lattice parameters 0.3951 nm [24] and 0.3927 nm [25], respectively) grown on TSO are subject to tensile strain. The substrate temperature during film growth was 500 °C, as measured by a thermocouple that is not in direct contact with the sample. The samples were vacuum annealed *in situ* (typically around  $10^{-8}$  Torr) at 510 °C for 30 min immediately after growth and cooled down to room temperature. The annealing step and the substrate-induced tensile strain are crucial for obtaining the IL phase without the presence of apical oxygen in the crystal structure [22, 23, 26]. The Sr and Cu shutter opening times were calibrated by monitoring RHEED oscillations during the growth of undoped SCO films, in order to obtain RHEED oscillations with constant maximum and minimum intensity. The RHEED patterns were observed using a glancing electron beam incident parallel to one of the in-plane [1 1 0]<sub>*p*</sub> azimuths of the substrate (the subscript indicates pseudo-cubic indices). After calibrating the shutter time, a SCO film was grown to measure the total film thickness using x-ray reflectivity (XRR). Determination of the SCO *c*-axis lattice spacing from XRD in combination with XRR on the same film provide a check of the actual number of deposited unit cells [22]. The equality between the number of shuttering periods and that of the actual number of unit cells grown is indicative of perfectly alternating complete Sr and CuO<sub>2</sub> monolayers. Finally, the growth of SLCO was achieved by opening the Sr shutter for 90% of the RHEED-calibrated time to deposit a full monolayer simultaneously with the La shutter open for 10% of the time required to deposit a full monolayer determined by a quartz crystal monitor (QCM). In order to confirm the actual La concentration in the grown SLCO film, we performed XRD and XPS analyses. XPS analysis corroborated the expected La concentration (0.1) within an experimental error of 12%, i.e. the La concentration is  $0.100 \pm 0.012$ .

The quality of the heterostructures deposited and the smoothness of their interfaces was also assessed by monitoring the RHEED pattern during growth. In figure 1(a), a typical RHEED pattern from the end of the growth of a SCO/SLCO/SCO trilayer sample is shown. It contains extra streaks, which disappear during the vacuum annealing step, figure 1(b). These extra streaks have been shown to be associated with a surface reconstruction related to excess oxygen [21]. They disappear as oxygen is removed during the vacuum annealing process.

Figure 2 shows high-angle annular dark field (HAADF) STEM images of a SLCO single layer calibration sample grown with the same deposition parameters used for SCO/SLCO/SCO trilayers. The stark Z-contrast between the heavy Tb A-sites in the substrate and the lighter Sr and La in the film, confirms the atomically abrupt TSO/SLCO interface, the high structural quality of the sample and the fully strained growth of the SLCO film, which in this case has a thickness larger than about 20 u.c.

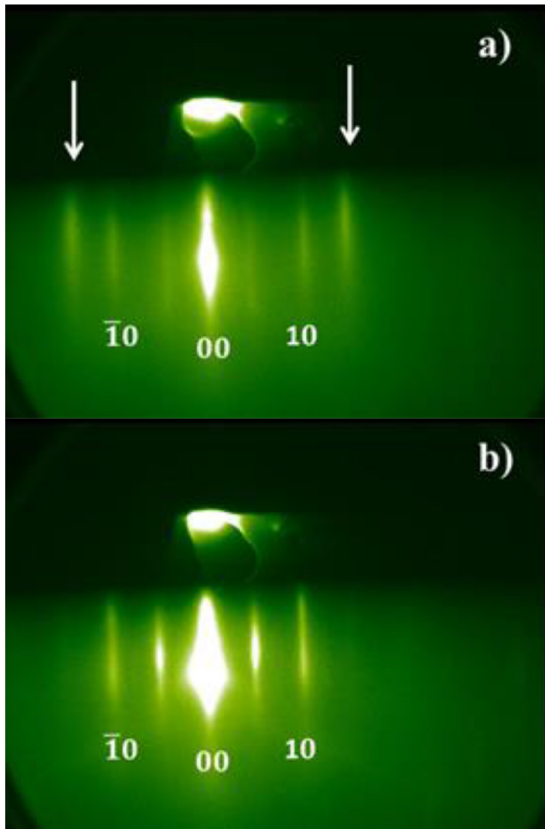


**Figure 1.** Typical RHEED pattern of an epitaxial trilayer viewed along the  $[1\ 1\ 0]_p$  azimuth at the end of growth (a) and after the vacuum annealing step (b). White arrows highlight extra diffraction streaks present in all as-grown films that disappear during vacuum annealing.

The samples were also structurally characterized by XRR and XRD in Bragg–Brentano  $\theta - 2\theta$  mode using Cu K- $\alpha$  radiation. In the case of the trilayered samples, the XRR measurements give information about the thickness of the central layers in the heterostructure and about the interface roughness. We have fitted the trilayer XRR curves using the Rigaku GXRR software (Rigaku Corporation, Tokyo, Japan) with the layers thickness, density and interface roughness as free fitting parameters. For the interface roughness we used a Gaussian profile; the standard deviation  $\sigma$  returned by the fitting routine was close to the unit cell value along the growth direction ( $\sim 0.34$  nm) for all the samples. The Levenberg–Marquardt fitting routine with statistical weighting of the logarithm of the data was used. As shown in figure 3, the intensity oscillations are clearly visible for scattering angles up to  $\theta = 4.5^\circ$ , confirming the low roughness of the surfaces and interfaces. In table 1, we summarize the results of the fitting procedure for all of the investigated trilayered samples.

The difference between the thickness of the top and bottom SCO layers was calculated by the fitting procedure and confirmed by the XRD measurements (see below).

In agreement with the calibration procedure and the shuttered period times used, the XRR measurements confirmed the bottom SCO thickness to be 20 u.c. and the top SCO layer to be 15 u.c., while the SLCO thickness varied from  $y = 20$  to  $y = 3$  ( $c\text{-axis}_{\text{SCO}} = 0.343$  nm,  $c\text{-axis}_{\text{SLCO}} = 0.340$  nm).

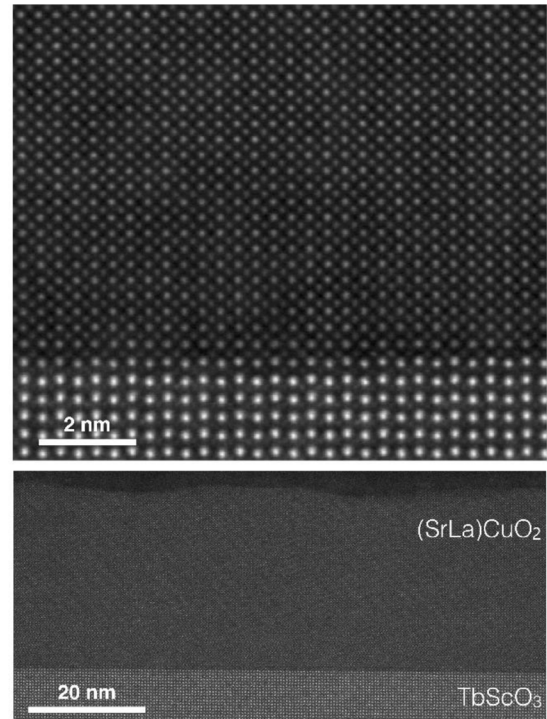


**Figure 2.** HAADF STEM images of a SLCO single-layer calibration sample grown with the same deposition parameters used for the SCO/SLCO/SCO trilayers. It is apparent that the interface is atomically abrupt and that the SLCO thin film has high structural quality.

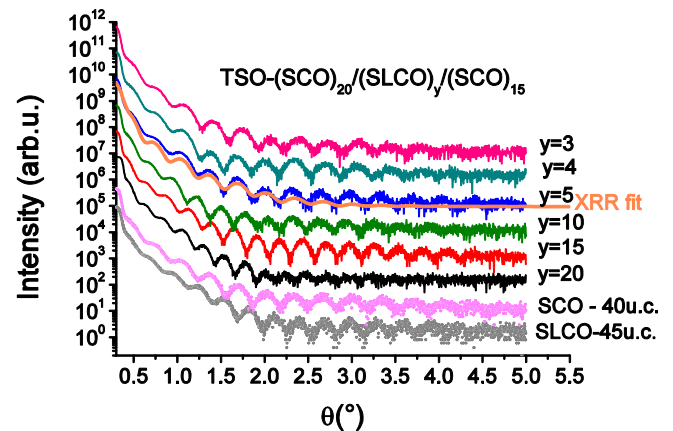


**Figure 3.** XRR intensity spectra as a function of the incident angle  $\theta$  of SCO and SLCO single layers as well as trilayers with different SLCO thickness ( $y = 20, 15, 10, 4$  and  $3$ ). A fit of the reflectivity is shown for the sample with  $y = 5$ . The data are offset along the  $y$ -direction for clarity.

In figure 4(a) XRD spectra of the same samples studied in figure 3 are shown. As outlined by the vertical dotted lines, the 200 diffraction peaks of the trilayers always fall in between the 200 peaks of the SCO and SLCO single films and progress, as expected, from the former to the latter with increasing  $y$ . In figure 4(b), the XRD simulation (GlobalFit–Rigaku Corporation, Tokyo, Japan) of the SLCO single layer (bottom curve) and of the trilayer  $(\text{SCO})_{20}/(\text{SLCO})_{20}/(\text{SCO})_{15}$  (top curve) is shown. The measured spectra result from the coherent addition of the contribution of each layer

**Table 1.** XRR fitting results for the trilayered samples investigated.

(SCO) <sub>20</sub> / (SLCO) <sub>y</sub> / (SCO) <sub>15</sub>	SCO bottom layer			SLCO central layer			SCO top layer		
	(Thick- ness ± 0.4) (nm)	(Density ± 0.6) (g cm <sup>-3</sup> )	(Rough- ness ± 0.1) (nm)	(Thick- ness ± 0.4) (nm)	(Density ± 0.6) (g cm <sup>-3</sup> )	(Rough- ness ± 0.1) (nm)	(Thick- ness ± 0.4) (nm)	(Density ± 0.6) (g cm <sup>-3</sup> )	(Rough- ness ± 0.1) (nm)
20/3/15	7.0	5.2	0.4	0.9	5.5	0.4	5.2	5.2	0.4
20/4/15	7.1	5.0	0.4	1.2	5.5	0.4	5.3	5.0	0.4
20/5/15	7.0	5.8	0.4	1.6	5.9	0.4	5.2	5.8	0.4
20/10/15	6.8	5.2	0.4	3.4	5.5	0.4	5.4	5.2	0.4
20/15/15	7.0	5.2	0.4	4.6	5.5	0.4	5.2	5.2	0.4
20/20/15	6.9	5.6	0.5	6.5	5.9	0.3	5.1	5.6	0.5

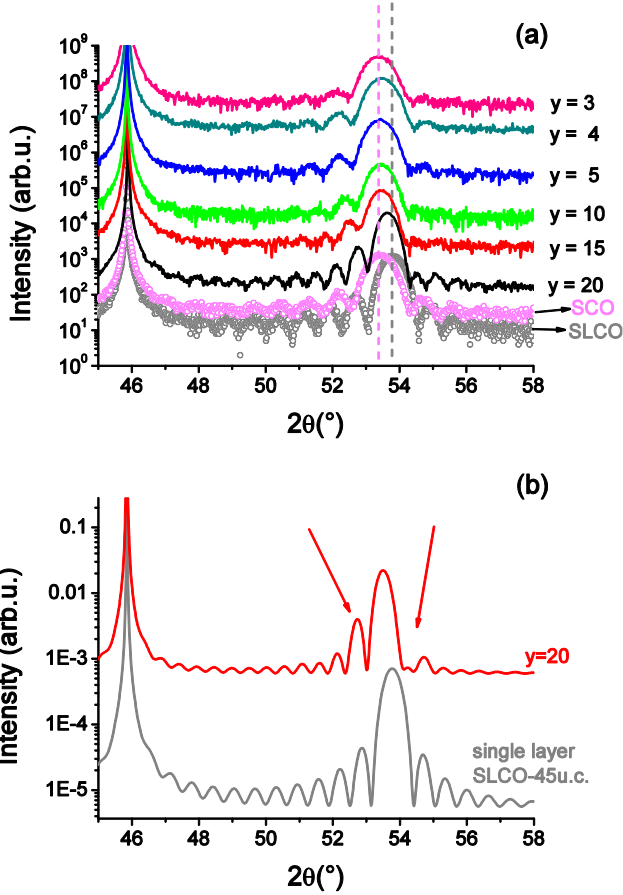


**Figure 4.** (a) XRD spectra of the same samples shown in figure 2; (b) simulation of the XRD spectra for the trilayer with SLCO  $y = 20$  (red curve) and SLCO single layer (grey curve).

of the heterostructure that gives rise to the interference pattern between top and bottom SCO layers and to the Laue fringes. This addition results in a visible asymmetry of the Laue fringes around the sample peaks in figure 4(a), which is clearly reproduced in the simulation curve (see arrows in figure 4(b)); the fringes around the SLCO single layer are more symmetric. Again, as expected, this asymmetry changes as the SLCO thickness,  $y$ , in the trilayers is lowered or the difference in the top and bottom SCO layer thickness is reduced.

The electrical transport properties of the trilayers with different  $y$  values were analyzed by performing sheet resistance measurements as a function of temperature using a van der Pauw four-probe geometry [27]. To make ohmic contacts, the

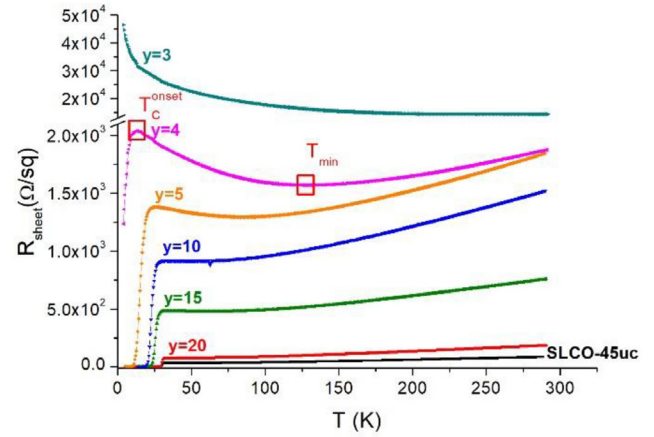


**Figure 5.** Sheet resistance  $R_{sheet}$  versus temperature  $T$  curves of trilayered samples with different SLCO layer thickness  $y$  in unit cells.  $T_C^{onset}$  and  $T_{min}$  are highlighted on the  $y = 4$  curve.

samples were scratched on the four corners of the SCO top layer, and the four points scratched were covered with pressed indium.

Structurally abrupt interfaces, as indicated by the XRR and XRD measurements, do not ensure by themselves the confinement of the charge carriers within the SLCO central layer. In the case of (SMO)<sub>20</sub>/(LSMO)<sub>15</sub>/(SMO) <sub>$z$</sub>  trilayers with varying  $z$  values, we have observed [17] that samples with  $z > 10$  showed values of metal-to-insulator transition temperature close to those expected for bulk LSMO.

SMO is a Mott insulator with an energy gap of 0.35 eV, while SCO has an energy gap higher than 1.2 eV [28]. This implies that for similar interface roughness and band alignment, that SCO should provide even better confinement of the charge carriers than SMO for a similar thickness.

Following our previous results [17], we therefore choose to deposit all of our SCO/SLCO/SCO trilayers with a topmost SCO layer thickness of 15 u.c.

In figure 5, the sheet resistance  $R_{sh}$  versus temperature  $T$  curves for the trilayers with varying center SLCO thicknesses are shown. The resistivity  $\rho$  of the SLCO layer has been estimated as:

$$\rho(T) = R_{sh} \cdot t_{SLCO}, \quad (1)$$

where  $t_{SLCO}$  is the thickness of the SLCO layer obtained by the XRR analysis. Typical errors related to  $R_{sh}$  values obtained using the van der Pauw method are around 10%–15% [27],

**Table 2.** Properties of the trilayer samples investigated with different SLCO layer thickness  $y$ .

$(y \pm 1)$ (u.c.)	$(T_C^{onset} \pm 2)$ (K) <sup>a</sup>	$(T_{min} \pm 0.5)$ (K)	$\rho_{RT}$ (m $\Omega$ cm) $\pm 30\%$	$R_{sh}^{RT}$ (k $\Omega$ ) $\pm 15\%$
20	32	—	0.12	0.19
15	31	61.5	0.34	0.8
10	30	49.0	0.5	1.5
5	23	83.0	0.3	1.8
4	13	128.0	0.2	1.9
3	Insulating	—	1.3	14

<sup>a</sup>  $T_C^{onset}$  is defined as the intersection of the straight lines describing the slope change before and after the superconducting transition.

and this could be the reason why samples with close  $y$  values (for example for  $y = 4$  and  $y = 5$ ) show very similar values of the room temperature sheet resistance and resistivity:  $R_{sh}^{RT}$  and  $\rho_{RT}$ , respectively (see table 2).

Similar to the case of SMO/LSMO/SMO  $p$ -doped trilayers, where we have considered the metal-to-insulator transition temperature [17], here we considered the superconducting transition temperature  $T_C$  as an additional check for evaluating the quality of the samples and interfaces produced. The  $T_C$  in SLCO thin films is generally dependent on many parameters (doping, disorder, strain, etc.) and can, therefore, be used as an additional parameter for evaluating the quality of the samples. The  $T_C$  of the trilayers shows a clear dependence on  $y$ . In particular, the  $T_C$  of the sample with  $y = 20$  is the same as that of the 45 u.c. thick SLCO single layer, while for  $y < 15$ ,  $T_C$  starts to decrease until it disappears for the sample with  $y = 3$ . For thicknesses  $4 \leq y < 20$ , an upturn in the  $R_{sh}$  values before the superconductive transition is observed, becoming more evident with decreasing SLCO thickness. In table 2 we summarize the main structural and transport parameters for the trilayered samples investigated. In the table,  $T_{min}$  is defined as the temperature at which the upturn (the local minimum in the curves) is observed.

### 3. Discussion

As mentioned in the previous section, the growth of SCO/SLCO/SCO trilayers with structurally abrupt interfaces, as confirmed by the STEM, XRR and XRD measurements, does not ensure by itself that the charge carriers are confined within the central SLCO layer. On the other hand, the observed superconducting behavior of the SLCO central layer gives the first indication of charge-carrier confinement due to the layering. The flat behavior of  $T_C$  versus  $y$  down to  $y = 10$  (see figure 6), with  $T_C$  values very close to the one observed in a single 45 u.c. thick SLCO film, strongly suggests that the charge carriers are indeed spatially confined within the SLCO layer. If the carriers were spread out in a large part of the trilayer thickness the effective doping of the system should strongly decrease with decreasing  $y$ , reaching values where the superconducting behavior is no longer expected. For example, if the charge were homogeneously spread over the entire trilayer,

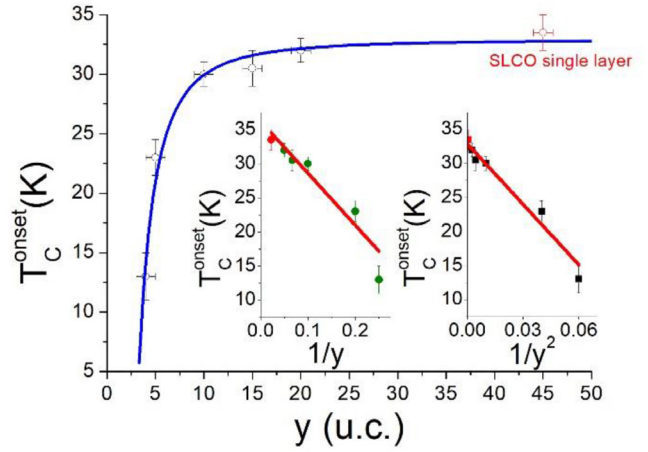


**Figure 6.** Critical onset temperature  $T_C^{onset}$  as a function of  $y$  where the blue curve is the best fit to equation (3). The inset shows the behavior and the linear fit (red lines) of  $T_C^{onset}$  as a function of  $1/y$  (left) and of  $1/y^2$  (right). Red dots highlight data from a single-layer film consisting entirely of SLCO.

the trilayer with  $y = 15$  ( $T_C = 30.5$  K) should have an effective doping smaller than 3% and not exhibit superconductivity [29]. The sudden drop in  $T_C$  observed for  $y < 10$  could also be related to the reduced dimensionality of the system induced by the layering. The influence of finite size on the order parameter of a second-order phase transition can be proven within a Ginzburg–Landau formalism as the one proposed in [30], where a surface term is added to the free energy functional compared to the standard approach. Following [30], one obtains that the critical temperature decreases with sample thickness  $t$  according to equation (2)

$$T_C(t) = T_{C_0} \left[ 1 - \left( \frac{L_0}{t} \right) \right], \quad (2)$$

where  $T_{C_0}$  represents the bulk critical temperature and  $L_0$  is the critical thickness below which a superconducting transition is no longer present.

While equation (2) has been shown to give good agreement with experimental data for dirty (disordered) superconductors, we have found that a better  $\chi^2$  value is obtained by equation (3)

$$T_C(t) = T_{C_0} \left[ 1 - \left( \frac{L_0}{t} \right)^2 \right], \quad (3)$$

which is based on a Ginzburg–Landau approach with conventional boundary conditions, appropriate to the case of a clean electronic system.

In the insets to figure 6, we show the behavior and the linear fits (red lines) of  $T_C$  as a function of  $1/y$  (left) and of  $1/y^2$  (right). Even though at a first glance the two fits do not appear very different, the comparison of the  $\chi^2$  values obtained by equations (2) and (3), 2.2 and 0.9 respectively, clearly indicates a better agreement for the case of the  $1/y^2$  dependence.

Equation (3) is equally applicable to ferromagnetic and superconductive phase transitions because both are described in terms of a generic order parameter  $f(z)$ , which is obtained from the slab free energy

$$F[f(z)] = S \int_{-t/2}^{t/2} dz [c(\partial_z f(z))^2 + af(z)^2 + bf(z)^4]$$

using the extremal condition  $\delta F[f(z)] = 0$  of variational calculus. Motivated by the slab geometry (defined by in-plane surface  $S$  and thickness  $t$ ), we assume that the order parameter only depends on the  $z$  coordinate because the system size is finite along this direction. Translational invariance is assumed along the plane perpendicular to the  $z$  direction. The extremal condition in combination with the usual boundary conditions  $\partial_z f(z)|_{z=\pm t/2} = 0$  leads to the differential equation for the order parameter  $\partial_z^2 f - \frac{a}{c}f = 0$ , where the non-linear term proportional to  $f^3$  has been omitted since it is negligible (compared to the linear term  $f$ ) at the phase transition temperature  $T^*$ . The solution of the differential equation is  $f = Ae^{i\mu z} + Be^{-i\mu z}$ , with  $\mu = \sqrt{\dot{a}(T_{C_0} - T^*)}/c$  and the temperature  $T^*$  obeys  $T^* < T_{C_0}$ . In deriving this result, we assume, as is usual applying the Ginzburg–Landau theory, that the coefficients  $b > 0$  and  $c > 0$  are temperature independent, while  $a = \dot{a}(T^* - T_{C_0})$  is a temperature-dependent quantity.

By applying the boundary conditions to  $f(z)$ , we obtain a set of two homogeneous equations for the arbitrary constants  $A$  and  $B$ . A non-trivial solution is found by insisting that the determinant of the coefficient matrix be zero; this condition leads to the equation  $\sin(\mu t) = 0$ , which results in solutions  $\mu t = n\pi$ , with  $n \in \mathbb{N}$ . Since the coefficient  $\mu$  is a function of temperature, the transition temperature of a system of finite thickness  $T^* = T_C(t)$  is a solution of the equation  $\mu(T^*)t = n\pi$ , where  $n$  is chosen to maximize the critical temperature  $T^* < T_{C_0}$ . Solving the equation for  $T^*$  and setting  $n = 1$ , we recover equation (3) with  $L_0 = \pi\sqrt{c}/(\dot{a}T_{C_0})$ . Therefore, the  $T_C(t)$  versus  $t$  curves strongly depend on the boundary conditions imposed by the Ginzburg–Landau treatment of the order parameter  $f(z)$  and thus the choice of adequate boundary conditions in describing a given physical system is a relevant problem. The better agreement that equation (3) gives to the experimental data in figure 6, suggests that disorder is not playing a major role in the sudden decrease of  $T_C$  with  $t$ . By fitting the data in figure 6 (blue curve), using equation (3), with  $T_{C_0}$  and  $L_0$  as free fitting parameters, we obtain  $T_{C_0} = (32.9 \pm 0.6) \text{ K}$  and  $L'_0 = L_0/z' = (3.0 \pm 0.1) \text{ u.c.}$ , where  $z'$  is the u.c. dimension along the  $z$  direction. The value for  $T_{C_0}$  is very close to the observed  $T_C$  for the single 45 u.c. thick SLCO film ( $T_C = 33 \text{ K}$ ) and the critical thickness  $L'_0 = 3 \text{ u.c.}$  agrees well with our observation that the  $y = 3$  sample is not superconducting.

The normal-state sheet resistance  $R_{sh}$  of the samples with  $3 < y < 20$  present an upturn at relatively low temperatures with a local minimum temperature  $T_{min}$ . For all the SCO/SLCO/SCO samples showing these minima, the  $T_{min}$  values are in the range 50–130 K (see table 2), and it is hard to explain their presence in terms of the emergence of quantum phenomena due to electronic mean free paths of the same order of magnitude as the inelastic dephasing length [31–33]. Our attempts to fit the  $R_{sh}$  curves in figure 5 over this temperature range (50–130 K), even allowing for a temperature dependence of

the dephasing inelastic scattering time failed, confirmed the inconsistency to the experimental data. We note that the  $T_{min}$  temperatures are close to the typical Néel temperatures measured in SLCO [29] and to the temperature at which a spin density-wave regime sets in for other electron-doped cuprate compounds [34]. Recently [7], *in situ* angle-resolved photoemission spectroscopy measurements on similar SLCO thin films, have shown the presence of a strong coupling between electrons and antiferromagnetic order at temperatures in the range of the observed  $T_{min}$ .

In figure 5, a sudden transition is observed in the normal state properties in going from the sample with  $y = 4$  to that with  $y = 3$ . The sample with  $y = 3$  does not have a  $T_{min}$ , does not show any metallic behavior ( $dR_{sh}/dT < 0$ ) and does not present any sign of a superconductive transition. In contrast, the sample with  $y = 4$  has a  $T_C^{onset}$  around 13 K, exhibits metallic behavior at high temperature and displays a  $T_{min}$  at about 120 K. Such a sudden transition from ‘metallic’ to ‘insulating’ behavior across a change of only one unit cell, is accompanied by a change of the  $R_{sh}$  low temperature values from about 2 k $\Omega$  to more than 30 k $\Omega$ . This transition from metallic to insulating behavior can be traced back to reaching a critical value of the low-temperature sheet resistance [35, 36].

Typically, in a fermionic scenario, where the charge carriers are treated as single electrons, a crossover is expected when a threshold value of  $R_{sh} = h/e^2 = 25.8 \text{ k}\Omega$  is reached. On the other hand, if a bosonic scenario holds, with charge carriers treated as pairs, the cross-over  $R_{sh}$  threshold value is  $R_{sh} = h/4e^2 = 6.45 \text{ k}\Omega$  [35, 36]. In any case, even assuming the validity of these models to explain the metal-insulator transition observed in our samples, the observed experimental data, with the ‘metallic’  $y = 4$  sample showing  $R_{sh} < 6.45 \text{ k}\Omega$  and the insulating  $y = 3$  one having  $R_{sh} > 25.8 \text{ k}\Omega$ , do not allow unambiguous discrimination between these two scenarios. Finally, for the trilayers with  $y = 3$  and 4 we have also analyzed the resistivity curves at low-temperatures (below 40 K).

Tentative fits of our resistivity data using temperature dependencies in agreement with different models (variable range hopping, semiconducting, Efros–Shklovskii, etc.) have always given a worse agreement compared to that obtained in terms of the quantum interference effects (QIE) picture. QIE and weak localization (WL) effects are expected to play an important role in the low temperature conductivity of layered metallic systems [37] and have been unambiguously observed in several layered compounds by electrical noise spectroscopy and by magnetoresistance measurements [33, 38–42].

If one assumes that QIEs are playing an important role in the low temperature electrical properties of our system, the observed temperature dependence can be traced back to the actual dimensionality of the electronic system. In fact, the quantum correction term introduced by QIE in the electrical conductivity is dependent on the system dimensionality. Specifically, a  $\ln(T)$  QIE term is expected for two-dimensional (2D) systems, while a power law contribution is at work for three-dimensional (3D) systems, with a specific  $T^{3/2}$

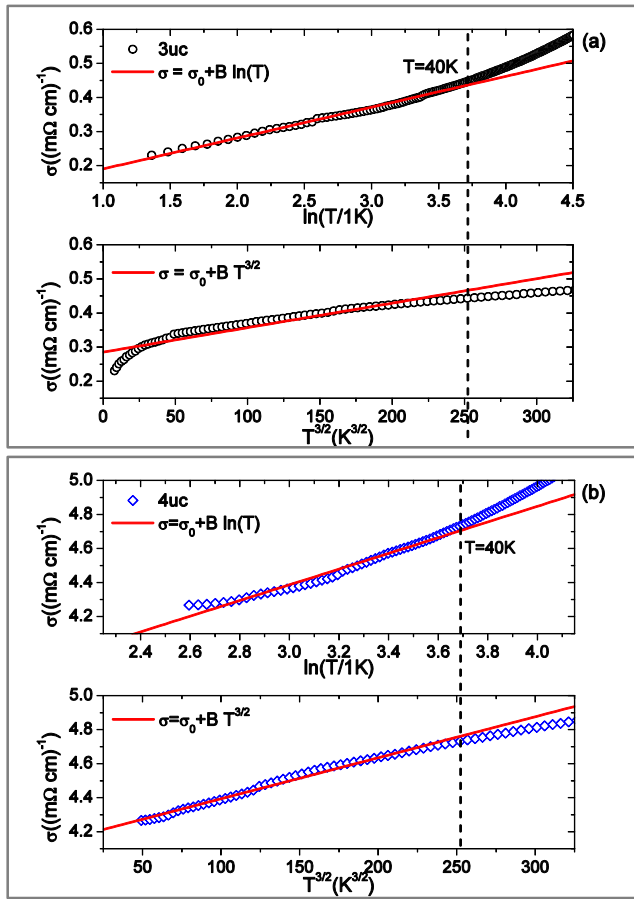


**Figure 7.** Linear fit (red curves) of the low temperature (below 40 K) conductivity of the sample with (a)  $y = 3$  and (b)  $y = 4$  as a function of  $\ln(T)$  (top) and  $T^{3/2}$  (bottom).

dependence in the case where the electron–phonon interaction is the mechanism affecting QIE [31].

In figure 7, the low-temperature conductivity  $\sigma = 1/\rho$  curves for the sample with  $y = 4$  (figure 7(a)) and  $y = 3$  (figure 7(b)) are plotted as a function of  $\ln(T)$  (bottom) and of  $T^{3/2}$  (top). The red curves in the figures are obtained following the best linear behavior as a function of  $\ln(T)$  and  $T^{3/2}$ , respectively. As is clear from the figures, see table 3, while the  $\sigma(T)$  curve for the  $y = 4$  sample follows a  $T^{3/2}$  dependence, that of the sample with  $y = 3$  shows better agreement to  $\ln(T)$  behavior. This sudden change from a  $T^{3/2}$  to a  $\ln(T)$  conductivity dependence observed in our trilayers going from  $y = 4$  to  $y = 3$ , suggests therefore a change in the dimensionality of the electronic system induced by the layering. Similar analysis performed over the same range of temperatures ( $T < 40$  K) on the samples with  $4 \leq y < 20$ , always yield conductivity behaviors better described by a  $T^{3/2}$  dependence.

When investigating the dimensionality of the transport properties in the normal state, the important parameter to compare to the SLCO thickness of the central layer is the electronic mean free path. Values of this parameter are generally quite difficult to experimentally define. Typical values given in the literature, are around 5 nm [43] which are of the same order as magnitude of the SLCO central layer thickness investigated in this work. Finally, we remark that STEM, XRD and

**Table 3.** Results of the linear fits presented in figure 7.

Central layer thickness	Temperature dependence	$R_{adj}^2$
$y = 3$	$\ln(T)$ dependence (2D)	0.997
	$T^{3/2}$ dependence (3D)	0.894
$y = 4$	$\ln(T)$ dependence (2D)	0.968
	$T^{3/2}$ dependence (3D)	0.997

XRR analysis all confirm the absence of structural disorder at the interfaces and that the  $T_C$  versus  $y$  behavior is better described in terms of electronically clean interfaces.

#### 4. Conclusion

SCO/SLCO/SCO trilayers have been grown by oxide MBE using a shuttered RHEED-calibrated layer-by-layer deposition process. STEM, XRR and XRD analyses confirm the structural quality and the abruptness of the interfaces of the deposited samples. The electrical transport properties of the trilayers with different SLCO thicknesses have been investigated as a function of temperature. The behavior of  $T_C$  as a function of SLCO layer thickness, with its sharp drop for  $y < 10$ , is well described in terms of a Ginzburg–Landau approach for a clean system with a finite size along growth direction. This gives a better agreement to the experimental data than other models based on dirty (disordered) systems. The normal state sheet resistance  $R_{sh}$  of the samples with  $3 < y < 20$  exhibit an upturn at relatively low temperatures with a local minimum temperature  $T_{min}$  in the range 50–130 K close to the typical Néel temperatures measured in SLCO. A sharp cross-over from metallic to insulating behavior has been observed going from the sample with  $y = 4$  to the one with  $y = 3$ , associated with a change in the temperature dependence of the conductivity curves from a  $T^{3/2}$  to a  $\ln(T)$  behavior. Such a change can be traced back, in a QIE scenario, to a change in the dimensionality of the electronic system going from 3D ( $y = 4$ ) to 2D ( $y = 3$ ). These results suggest the presence, in the investigated electron-doped SCO/SLCO/SCO trilayers, of layering induced spatial charge carrier confinement influencing the normal state transport properties of the system. These findings, associated to the results of our previous work on  $p$ -doped trilayers open the door to new developments in the growth of  $n$  and  $p$  doped oxide-based QWs and quantum devices.

#### Acknowledgments

The work at Cornell was supported by the National Science Foundation (NSF) under Grant No. DMR-1610781. The Platform for the Accelerated Realization, Analysis, and Discovery of Interface Materials (PARADIM) under Cooperative Agreement No. DMR-1539918. This work made use of the Cornell Center for Materials Research with funding from the NSF MRSEC program (DMR-1719875). Additional support was provided by the Department of Defence Air Force Office of Scientific Research under award number FA 9550-16-1-0305. The FEI Titan Themis 300 was acquired through NSF-MRI-1429155, with additional support from Cornell



University, the Weil Institute and the Kavli Institute at Cornell. Substrate preparation was performed in part at the Cornell NanoScale Facility Science and Technology, a member of the National Nanotechnology Coordinated Infrastructure (NNCI), which is supported by the NSF (Grant No. ECCS-1542081).

## ORCID iDs

Chiara Sacco  <https://orcid.org/0000-0002-1227-4979>

## References

- [1] Ohtomo A and Hwang H Y 2004 A high-mobility electron gas at the  $\text{LaAlO}_3/\text{SrTiO}_3$  heterointerface *Nature* **427** 423–7
- [2] Bibes M, Villegas J E and Barthélémy A 2011 Ultrathin oxide films and interfaces for electronics and spintronics *Adv. Phys.* **60** 5–84
- [3] Biscaras J, Bergeal N, Kushwaha A, Wolf T, Rastogi A, Budhani R C and Lesueur J 2010 Two-dimensional superconductivity at a Mott insulator/band insulator interface  $\text{LaTiO}_3/\text{SrTiO}_3$  *Nat. Commun.* **1** 1–5
- [4] Zhai X F, Mohapatra C S, Shah A B, Zuo J M and Eckstein J N 2010 New optical absorption bands in atomic-layer superlattices *Adv. Mater.* **22** 1136–9
- [5] Choi W S, Jeong D W, Seo S S A, Lee Y S, Kim T H, Jang S Y, Lee H N and Myung-Whun K 2011 Charge states and magnetic ordering in  $\text{LaMnO}_3/\text{SrTiO}_3$  superlattices *Phys. Rev. B* **83** 195113
- [6] Galdi A, Aruta C, Orgiani P, Adamo C, Bisogni V, Brookes N B, Ghiringhelli G, Schlom D G, Thakur P and Maritato L 2012 Electronic band redistribution probed by oxygen absorption spectra of  $(\text{SrMnO}_3)_n(\text{LaMnO}_3)_{2n}$  superlattices *Phys. Rev. B* **85** 125129
- [7] Harter J W, Maritato L, Shai D E, Monkman E J, Nie Y, Schlom D G and Shen K M 2012 Nodeless superconducting phase arising from a strong ( $\pi$ ,  $\pi$ ) antiferromagnetic phase in the infinite-layer electron-doped  $\text{Sr}_{1-x}\text{La}_x\text{CuO}_2$  compound *Phys. Rev. Lett.* **109** 267001
- [8] Stemmer S and Millis A J 2013 Quantum confinement in transition metal oxide quantum wells *MRS Bull.* **38** 1032–9
- [9] Schlom D G, Haeni J H, Lettieri J, Theis C D, Tian W, Jiang J C and Pan X Q 2001 Oxide nano-engineering using MBE *Mater. Sci. Eng. B* **87** 282–91
- [10] Biegalski M D et al 2008 Critical thickness of high structural quality  $\text{SrTiO}_3$  films grown on orthorhombic (101)  $\text{DyScO}_3$  *J. Appl. Phys.* **104** 114109
- [11] Jalan B, Engel-Herbert R, Wright N J and Stemmer S 2009 Growth of high-quality  $\text{SrTiO}_3$  films using a hybrid molecular beam epitaxy approach *J. Vac. Sci. Technol. A* **27** 461–4
- [12] Petrov A Y, Aruta C, Mercione S, Adamo C, Alessandri I and Maritato L 2004 Room temperature metal–insulator transition in as grown  $(\text{La}_{1-x}\text{Sr}_x)_y\text{MnO}_3$  thin films deposited by molecular beam epitaxy *Eur. Phys. J. B* **40** 11–7
- [13] Moetakef P, Jackson C A, Hwang J, Balents L, Allen S J and Stemmer S 2012 Toward an artificial Mott insulator: Correlations in confined high-density electron liquids in  $\text{SrTiO}_3$  *Phys. Rev. B* **86** 201102
- [14] Nemšák S et al 2015 Observation by resonant angle-resolved photoemission of a critical thickness for 2-dimensional electron gas formation in  $\text{SrTiO}_3$  embedded in  $\text{GdT}_2\text{O}_3$  *Appl. Phys. Lett.* **107** 231602
- [15] Jackson C A, Zhang J Y, Freeze C R and Stemmer S 2014 Quantum critical behaviour in confined  $\text{SrTiO}_3$  quantum wells embedded in antiferromagnetic  $\text{SmT}_2\text{O}_3$  *Nat. Commun.* **5** 1
- [16] Yoshimatsu K, Horiba K, Kumigashira H, Yoshida T, Fujimori A and Oshima M 2011 Metallic quantum well states in artificial structures of strongly correlated oxide *Science* **333** 319–22
- [17] Galdi A, Sacco C, Orgiani P, Romeo F and Maritato L 2017 Growth and characterization of charge carrier spatially confined  $\text{SrMnO}_3/\text{La}_{0.7}\text{Sr}_{0.3}\text{MnO}_3/\text{SrMnO}_3$  trilayers *J. Cryst. Growth* **459** 56–60
- [18] Søndena R, Ravindran P, Stølen S, Grande T and Hanfland M 2006 Electronic structure and magnetic properties of cubic and hexagonal  $\text{SrMnO}_3$  *Phys. Rev. B* **74** 144102
- [19] Millis A J and Schlom D G 2010 Electron-hole liquids in transition-metal oxide heterostructures *Phys. Rev. B* **82** 073101
- [20] Kim H M, Kim U, Park C, Kwon H and Char K 2016 Thermally stable pn-junctions based on a single transparent perovskite semiconductor  $\text{BaSnO}_3$  *APL Mater.* **4** 056105
- [21] Harter J W, Maritato L, Shai D E, Monkman E J, Nie Y, Schlom D G and Shen K M 2015 Doping evolution and polar surface reconstruction of the infinite-layer cuprate  $\text{Sr}_{1-x}\text{La}_x\text{CuO}_2$  *Phys. Rev. B* **92** 035149
- [22] Maritato L, Galdi A, Orgiani P, Harter J W, Schubert J, Shen K M and Schlom D G 2013 Layer-by-layer shuttered molecular-beam epitaxial growth of superconducting  $\text{Sr}_{1-x}\text{La}_x\text{CuO}_2$  thin films *J. Appl. Phys.* **113** 053911
- [23] Karimoto S and Naito M 2004 Electron-doped infinite-layer thin films with  $T_C^{\text{zero}} = 41$  K grown on  $\text{DyScO}_3$  substrates *Physica C* **412–4** 1349–53
- [24] Hiroi Z, Azuma M, Takano M and Bando Y 1991 A new homologous series  $\text{Sr}_{n-1}\text{Cu}_{n+1}\text{O}_{2n}$  found in the  $\text{SrO-CuO}$  system treated under high pressure *J. Solid State Chem.* **95** 230–8
- [25] Jorgensen J D, Radaelli P G, Hinks D G, Wagner J L, Kikkawa S, Er G and Kanamaru F 1993 Structure of superconducting  $\text{Sr}_{0.9}\text{La}_{0.1}\text{CuO}_2$  ( $T_c = 42$  K) from neutron powder diffraction *Phys. Rev. B* **47** 14654–6
- [26] Galdi A et al 2018 X-ray absorption spectroscopy study of annealing process on  $\text{Sr}_{1-x}\text{La}_x\text{CuO}_2$  electron-doped cuprate thin films *J. Appl. Phys.* **123** 123901
- [27] Van der Pauw I J 1958 A method of measuring specific resistivity and Hall effect of discs of arbitrary shape *Philips Res. Rep.* **13** 1–9
- [28] Popovic Z V et al 2001 Optical studies of gap, hopping energies and the Anderson-Hubbard parameter in the zigzag-chain compound  $\text{SrCuO}_2$  *Phys. Rev. B* **63** 165105
- [29] Armitage N P, Fournier P and Greene R L 2010 Progress and perspective on electron-doped cuprates *Rev. Mod. Phys.* **82** 2421
- [30] Simonin J 1986 Surface term in the superconductive Ginzburg–Landau free energy: application to thin films *Phys. Rev. B* **33** 7830–2
- [31] Lee P A and Ramakrishnan T V 1985 Disordered electronic systems *Rev. Mod. Phys.* **57** 287–337
- [32] Maritato L, Adamo C, Barone C, De Luca G M, Galdi A, Orgiani P and Petrov A Y 2006 Low-temperature resistivity of  $\text{La}_{0.7}\text{Sr}_{0.3}\text{MnO}_3$  ultra thin films: role of quantum interference effects *Phys. Rev. B* **73** 094456
- [33] Orgiani P, Galdi A, Sacco C, Arpaia R, Charpentier S, Lombardi F, Barone C, Pagano S, Schlom D G and Maritato L 2015 The role of quantum interference effects in normal-state transport properties of electron-doped cuprates *J. Supercond. Nov. Magn.* **28** 3481–6
- [34] Jin K, Zhang X H, Bach P and Greene R L 2009 Evidence for antiferromagnetic order in  $\text{La}_{2-x}\text{Ce}_x\text{CuO}_4$  from angular magnetoresistance measurements *Phys. Rev. B* **80** 012501

- [35] Liu Y, McGreer K A, Nease B, Haviland D B, Martinez G, Halley J W and Goldman A M 1991 Scaling of the insulator-to-superconductor transition in ultrathin amorphous Bi films *Phys. Rev. Lett.* **67** 2068–71
- [36] Orgiani P, Aruta C, Balestrino G, Born D, Maritato L, Medaglia P G, Stornaiuolo D, Tafuri F and Tebano A 2007 Direct measurement of sheet resistance  $R_{sq}$  in cuprate systems: evidence of a fermionic scenario in a metal-insulator transition *Phys. Rev. Lett.* **98** 036401
- [37] Kennett M P and McKenzie R H 2008 Quantum interference and weak localization effects in the interlayer magnetoresistance of layered metals *Phys. Rev. B* **78** 024506
- [38] Barone C, Romeo F, Galdi A, Orgiani P, Maritato L, Guarino A, Nigro A and Pagano S 2013 Universal origin of unconventional  $1/f$  noise in the weak-localization regime *Phys. Rev. B* **87** 245113
- [39] Barone C, Guarino A, Nigro A, Romano A and Pagano S 2009 Weak localization and  $1/f$  noise in  $\text{Nd}_{1.83}\text{Ce}_{0.17}\text{CuO}_{4+6}$  thin films *Phys. Rev. B* **80** 224405
- [40] Rullier-Albenque F, Alloul H and Tourbot R 2001 Disorder and transport in cuprates: weak localization and magnetic contributions *Phys. Rev. Lett.* **87** 157001
- [41] Niu W, Gao M, Wang X, Song F, Du J, Wang X, Xu Y and Zhang R 2016 Evidence of weak localization in quantum interference effects observed in epitaxial  $\text{La}_{0.7}\text{Sr}_{0.3}\text{MnO}_3$  ultrathin films *Sci. Rep.* **6** 26081
- [42] Barone C, Galdi A, Sacco C, Orgiani P, Schlom D G, Pagano S and Maritato L 2016 Noise spectroscopy investigation of interplay between quantum interference effects and superconductivity in infinite layer cuprates *IEEE Trans. Appl. Supercond.* **26** 1–4
- [43] Fruchter L, Bouquet F and Li Z Z 2012 Zero-bias anomalies on  $\text{Sr}_{0.88}\text{La}_{0.12}\text{CuO}_2$  thin films *Physica C* **483** 213–6